# Morphological Alterations during Texture-Producing Plastic Plane Strain Compression of High-Density Polyethylene

**A. Galeski**

*Centre of Molecular and Macromolecular Studies, Polish Academy of Sciences, 90-363 Lodz, Poland*

**Z. Bartczak,† A. S. Argon,* and R. E. Cohen***

*Massachusetts Institute of Technology, Cambridge, Massachusetts 02139*

*Received January 18, 1992; Revised Manuscript Received May 21, 1992*

ABSTRACT: Numerous specimens of a single linear polyethylene sample were deformed by plane strain compression in a channel die to very large plastic strains. The mechanisms of deformation were elucidated by density measurements, polarized light microscopy, transmission electron microscopy, and wide-angle and small-angle X-ray diffraction. A deconvolution procedure for separating overlapping X-ray diffraction peaks and the diffuse scattering from the amorphous material was also applied, and pole figures were reconstructed from the corrected data. At a compression ratio of 1.80 intense shear localization appeared at ±45° with respect to the flow direction. There is strong evidence for interlamellar sliding only at low compression ratios. Once this sliding is apparently exhausted, crystallographic slip on the (100)[001] chain slip system sets in. At a compression ratio above 1.80 and 3.13 respectively, (100)[010] transverse slip and (010)[001] chain slip processes are observed. The strong shear bands occurring at compression ratios of 2.5 and 3.13 originated mainly from (100)[001] and (100)[010] slip processes. The morphology at a compression ratio of 6.44 resembles a monocrystal texture. Further deformation occurs by (100)[001] slip and to a lesser extent by (010)[001] chain slip. The (110) twinning process shows limited activity, but only at very high compression ratios near 12. Associated TEM studies have shown that while the initial amorphous material layers attached to the lamellae rotate to lie normal to the loading direction, a new long period starts to evolve normal to the flow direction beginning at a compression ratio of 3.13; this new long period forms via an apparent widespread pinch-off of stretched lamellae and translation of interfaces above a compression ratio of 3.13 and becomes progressively better defined with continued deformation. It is suggested that the breakup of thinned lamellae is due to a deformation instability related to the increase of interface stretching resistance of the crystalline and amorphous layers and is initiated by thickness irregularities. Because of defects (tie links, etc.) that have good mobility along the chain in the newly evolved amorphous material, the fully textured quasi-crystal sample has a continuous background of crystals with layers of segregated chain defects making up the new long period. There is also some evidence for the formation of flaws and fissures in planes perpendicular to the load direction, which causes brittleness in tension associated with fracture along the (100) planes.

## I. Introduction

It is now well established that the plastic deformation of semicrystalline polymers involves several mechanisms of deformation of crystalline and amorphous phases (see e.g. ref 1). Among them slip along certain crystallographic planes, twinning, martensitic transformations, interlamellar sliding, and even lamellar separation are the most widely reported processes. Although crystals may undergo slip in the chain direction readily, they are inextensional in the chain direction. Possible plastic deformation mechanisms in such crystals were summarized earlier by Bowden and Young[2] and by Haudin,[3] and have recently been reviewed by Lin and Argon.[4]

Theoretical considerations, supported by experimental observation of the deformation of single crystals, led to the conclusion that chain slip along any of the (*hk*0) planes in the direction of the [001] molecular axis is kinematically possible. The general rule is that slip occurs on the most closely packed crystallographic planes and in the most closely packed direction in these planes. It was expected from considerations of interfacial energy that the slip processes along the (100), (010), and (110) planes are the most probable.[5] Experimental studies have shown that the two most important chain slip modes are (100)[001] and (010)[001].[2,3] The third slip system along the (110) plane, although widely postulated, has not been detected experimentally. In the recent study of Bartczak, Argon, and Cohen[6] the (100)[001] and (010)[001] chain slip (100)-[010] transverse slip processes were identified as the dominant active slip systems in polyethylene. The respective critical shear stresses were directly determined in mechanical shear tests as 7.2, 15.6, and 12.2 MPa, respectively, at room temperature. In addition {110} twinning and the $T1_2$ stress-induced martensitic transformation are also known to be active modes of plastic deformation for certain particular orientations of polyethylene crystals. At room temperature these two mechanisms occur at approximately 14 MPa of resolved shear stress.[7] The (110)[001] chain slip and (010)[100] and (110)[1$\bar{1}$0] transverse slip processes were excluded by Bartczak et al.[6] as inactive deformation mechanisms in simple shear.

For the amorphous phase, two modes of plastic deformation have been proposed; interlamellar sliding and lamellar separation.[8,9] While the preferred process of lamellar sliding is properly descriptive, it gives no information about the chain rearrangement within the amorphous region. Since the nature of the amorphous material, in thin layers between lamellae, is not well-known, the mechanism of plastic deformation in the amorphous region is presently not well understood. Nevertheless, the kinetic aspects are well represented by a molecular level model of Argon[10] which has recently been generalized and implemented in computational application by Boyce, Parks, and Argon.[11]

† Permanent address: Centre of Molecular and Macromolecular Studies, Polish Academy of Sciences, 90-363 Lodz, Poland.

0024-9297/92/2225-5705$03.00/0 

The intensity of each deformation mechanism depends on the type of polymer, its crystallographic unit cell, the initial morphology of the material (i.e. the orientation of the crystals with respect to the applied stresses, their dimensions, the short- and long-range correlation of crystal arrangement, and degree of crystallinity), and the conditions of the deformation test, e.g. the rate, the temperature, the pressure, and the size and shape of the specimen.

It was found long ago that initially spherulitic polyethylene in bulk undergoes extensive changes during plastic straining. In the case of thin films Hay and Keller[12] found that in regions of the spherulite where the radius vector is nearly perpendicular to the draw direction, i.e. in the equatorial zones of the spherulites, the deformation is in the form of an extension of material accompanied by some compression in the transverse direction. The portion of the spherulites that makes up the 45° fans rotates toward the poles while polar regions of the spherulites are extended along the drawing direction. From the earlier studies of Peterlin[13,14] the prevailing picture for plastic deformation of a semicrystalline polymer has been stated as the destruction of lamellae associated with their unraveling and transformation into densely packed microfibrils, all thought to occur in a catastrophic process termed "micronecking". We will demonstrate below and also in an associated-computer simulation[15] that this prevailing picture must be substantially modified.

Polyethylene samples deformed to a high deformation ratio in the course of plane strain compression develop an interesting texture that closely resembles a monocrystal.[6,16] Although the details of the morphology of such samples are already well-known, the routes through which the initially spherulitic morphology approaches the monocrystal texture is understood only in a very rough outline. In this report we present the results of a new study of the mechanisms of deformation of a single bulk high-density polyethylene in plane strain compression in a channel die. Channel die compression is kinematically very similar to plane strain tension. It results in uniaxial flow of the polymer in plane strain; however, being under compression, it avoids internal cavitation and all the attendant artifacts such as the micro-necking process that are inessential for the understanding of the large strain texture formation process. Therefore, the material strained in the channel die changes shape by a continuous series of transformations without cavitation, and this fact permits obtaining deformed samples for detailed study, within the whole spectrum of strains. The process of deformation is, however, subject to shear localization and to a ubiquitous process of lamella pinch-off beginning at a compression ratio of 3.13 that permits the establishment of a new long period.

## II. Experimental Section

High-density polyethylene (Petrothene LS 606–00, Quantum, USI Division, Cincinnati, OH) was used in this study. Its weight-average molecular weight, $M_w$, was 55 000, polydispersity index, $M_w/M_n$, 4.80, melt flow index 9–11 g/10 min (ASTM D-1238-57T), and density in the range 0.941–0.980 g/cm$^3$ depending on its degree of crystallinity. Plaques of 12-mm thickness, 125-mm length, and 74-mm width were obtained by compression molding at 180 °C and 100 atm pressure. The mold assembly was slowly cooled to room temperature over a period of several hours. The outer layers of the plaques were removed by machining and several samples of 74-mm length, 10-mm thickness, and various widths were cut from the plaques for further studies. All surfaces of the samples were covered with Dow Corning high-temperature ball bearing grease for reducing friction in the channel die.

A channel die, the description of which was given in detail elsewhere,[16–18] was used for performing the plane strain compression. This channel die was similar in design to that used by Gray et al.[19] The temperature of the channel die was maintained at 80 °C during the compression flow. The load was applied continuously with a deformation rate of 0.0025 s$^{-1}$ until the desired compression ratios were achieved. In order to study the course of deformation and the corresponding changes in morphology, samples were compressed to different compression ratios and then cooled to room temperature under load, followed by load release. The final compression ratio was determined from the reduction of the cross section of the samples. Samples having compression ratios of 1.16, 1.34, 1.55, 1.80, 2.50, 3.13, 4.16, 6.44, and 12.1 were prepared in this manner.

Densities of the samples were determined by means of a density gradient column. The 1-m-high column, covering the range from 0.800 to 0.990 g/cm$^3$, was filled with a mixture of ethyl alcohol and water. All measurements were performed at 22 °C. The readout of the positions of the samples in the column was taken 15 min to 3 weeks after introducing the samples.

A Rigaku X-ray diffractometer with computerized pole figure attachment was employed in the study. The Cu K$\alpha$ line generated at 50 kV and 60 mA from a rotating-anode point source was filtered using electronic filtering and the usual thin Ni filter. The X-ray diffractometer and pole figure attachment were controlled on-line by means of a dedicated MicroVAX computer running under DMAXB Rigaku-USA software. The slit system that was used allowed for collection of the diffracted beam with a divergence angle of less than 0.3°. Complete pole figures were obtained for projections of Euler angles of sample orientation with respect to the incident beam, $\alpha$ from 0 to 90° in 5° steps and $\beta$ from 0 to 360° also in 5° steps. The specimens (1.3 mm thick) for X-ray investigations were cut from the oriented samples perpendicular to the flow direction, and several of them were assembled to form an approximately 2-cm × 2-cm flat square piece. The following diffraction reflections from the orthorhombic crystal structure of polyethylene were of special interest: (200), (020), (002), and (110). The (200) and (110) reflections are superimposed on the amorphous halo for $2\theta$ angles from 13 to 27°, the (020) reflection appears at $2\theta$ angles from 33 to 38°, and the (002) reflection appears in the range from 72 to 76°. The construction of full pole figures required the connection of X-ray data from the transmission and reflection modes. The connecting angle $\alpha$ was 45° for $2\theta$ angles below 38°, and $\alpha$ = 30° was used for $2\theta$ angles above 72°. Due to significant broadening and overlapping of X-ray reflections in polyethylene, the measured diffracted intensity at any particular $2\theta$ angle is often a superposition of intensities from several peaks and the amorphous halo. Interpretation of the pole figure constructed from such data is not straightforward, and therefore, the X-ray data for $2\theta$ in the range from 13 to 27° were all deconvoluted in the manner we have introduced in an earlier set of communications on Nylon 6.[18,20] Only the background was subtracted from the recorded intensities at all other $2\theta$ angles. Pole figures from the set of data for peak widths were also constructed (for details see refs 18 and 20). These peak width pole figures are best interpreted as contours of the X-ray diffraction peak width of that population of crystals which is oriented at Euler angles $\alpha$ and $\beta$. The corresponding relative amount of these same crystals is given by the corresponding peak intensity pole figure. Within the specific limitation resulting from broadening of X-ray reflections due to residual stresses, the peak width can be treated as a qualitative measure of the mean size of undisturbed crystal structure. The pole figure of peak widths is in fact a map of X-ray-averaged sizes of regions with undisturbed crystal structure. We also used the deconvoluted X-ray data to determine the degree of crystallinity in the samples by integrating intensities in a respective pole figure for each X-ray reflection and for the amorphous halo.

The morphologies of the original and the compressed samples were examined by polarized light microscopy in 1-$\mu$m-thick sections cut perpendicular to the flow direction and parallel to the compression (loading) direction. These thin samples were sectioned using a LKB Ultromicrotome V equipped with glass knives. For the purpose of reducing plastic deformation during microtoming and ultramicrotoming and of improving contrast in transmission electron microscopy studies, all the undeformed and deformed samples were first fixed and stained in chlorosulfonic acid at 60 °C for 20 h according to the original procedure described by Kanig.[21] The stained samples were ultramicrotomed perpendicular to the constrained direction. Ultrathin sections

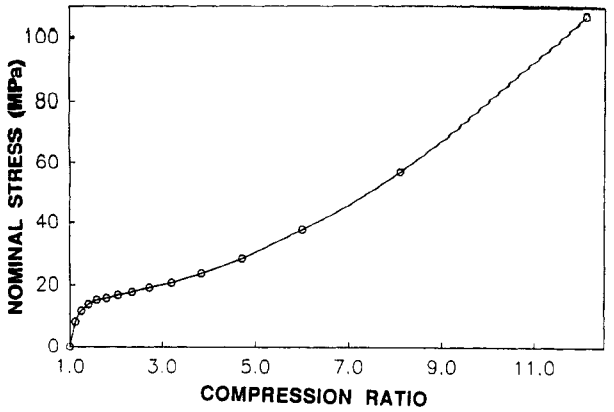


**Figure 1.** Load-compression ratio curve for a 74-mm-wide linear polyethylene sample compressed in a channel die with the deformation rate of 0.0025 $s^{-1}$.

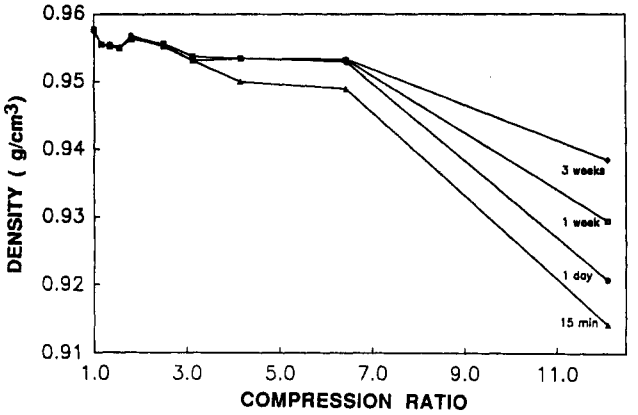


**Figure 2.** Density change of linear polyethylene samples subjected to plane strain compression in a channel die vs the compression ratio determined from sample position in a gradient column after a specified time lapse.

were placed on copper grids and covered with a thin carbon film for better antistatic discharge and better mechanical support. The sections were then examined using a Phillips 300 transmission electron microscope operating at 100 kV. The changes in lamellae due to deformation were also studied by means of small-angle X-ray scattering (SAXS). The SAXS measurements were performed on a computer-controlled system consisting of a Nicolet two-dimensional position-sensitive detector associated with a Rigaku rotating-anode generator operating at 40 kV and 30 mA and providing Cu K$\alpha$ radiation. The primary beam was collimated by two Ni mirrors. The specimen to detector distance was 2.3 m. The scattered beam path between the specimen and the detector was enclosed by an Al tube filled with helium gas in order to minimize the background scattering.

## III. Results

**3.1. Stress–Strain Experiments and Density Changes.** The load-compression ratio curve for a 74.0-mm-wide polyethylene sample compressed in a channel die at 80° is plotted in Figure 1. The initial elastic response of the sample is followed by the region of intense plastic deformation and flow with only moderate hardening. At compression ratios above 4.0 strain hardening is seen to increase.

The density change of polyethylene samples subjected to compression in the channel die is presented in Figure 2 as a function of the compression ratio (curve marked 15 min). An initial slight decrease of the density is followed by a small increase; then above a compression ratio of 2.0 there is a monotonic decrease in density. Comparison of Figure 1 with Figure 2 reveals that the initial decrease in density is correlated with the initial elastic response of the sample. The subsequent increase of the density can be ascribed to the beginning of an intense yielding process

**Table I**
**Degrees of Crystallinity of Compressed Linear Polyethylene Samples**

| compression ratio | crystallinity | compression ratio | crystallinity |
|---|---|---|---|
| 1.0 | 0.645 | 3.13 | 0.532 |
| 1.8 | 0.584 | 6.44 | 0.526 |
| 2.53 | 0.582 | | |

taking place at a compression ratio above 1.5. Further decrease of the density above a compression ratio of 2.0 can be at least partially attributed to the formation of some porosity during deformation, since soaking these samples in the gradient column liquid for longer times (Figure 2, curves marked 1 day and 3 weeks) results in a substantial increase of their apparent density.

The degrees of crystallinity of undeformed and deformed samples, as obtained by X-ray diffraction, using the overlapping peak separation procedure followed by integration, are presented in Table I. It is seen that crystallinity is at a maximum in the initial sample. At the compression ratio of 1.8, the sample crystallinity (orthorhombic) is about 58%. As the compression ratio increases to 2.5 the crystalline fraction remains almost constant. Compression above 2.5 results in a rapid decrease of the crystalline content. Further compression causes only a slight further decrease of the degree of crystallinity.

**3.2. Morphological Alterations.** Polarized light micrographs of thin sections of the initial fixed and stained material and the compressed fixed and stained samples are presented in Figure 3a–i. The undeformed sample (Figure 3a) exhibits well-developed spherulitic structure. In sections normal to the constraint direction (Figure 3b,c) the spherulites appear elongated along the flow direction as the compression ratio increases. However, at a compression ratio of 1.8 (Figure 3d) clear spherulitic arrangement can no longer be distinguished in these sections. Above this compression ratio intense, coarse shear bands at ±45° with respect to the flow direction appear at roughly 300-$\mu$m spacing. In the sample with compression ratio 2.5 (Figure 3e) the regions between these coarse shear bands become filled with a very dense collection of fine shear bands with an average spacing of approximately 1–3 $\mu$m. There is no evidence that any of the shear bands are formed at former spherulite boundaries. A further increase of the compression ratio does not cause any significant increase in the number of shear bands. Instead, as a result of overall quasi-homogeneous compression, the shear bands generated at lower compression ratios become tilted toward the flow direction at higher compression ratios, as is seen in Figure 3g–i for compression ratios 4.16, 6.44, and 12.1.

Parts a–g of Figure 4 show transmission electron micrographs of ultrathin sections of deformed samples of various compression ratios, sliced normal to the constraint direction. In the undeformed sample and in deformed samples with increasing compression ratios of 1.16, 1.80, 2.50, 3.13, 6.00, and 6.44, a clear lamellar structure can always be distinguished. In undeformed samples the lamellae are oriented at all possible angles. The ultrathin section of such a sample reveals images of lamellae cut randomly. The thickness of cut lamellae, together with the adjacent amorphous layer as seen in TEM varies from 150 to 220 Å. In the sample with compression ratio 1.8, rows of kinked lamellae can be identified. These lamellae have previously been oriented with their normals perpendicular to the loading direction. Perhaps that kinking contributes to the further development of shear bands, observed at higher compressions.

In micrographs of ultrathin sections of samples with compression ratios 2.50 and 3.13, the lamellae tend to orient

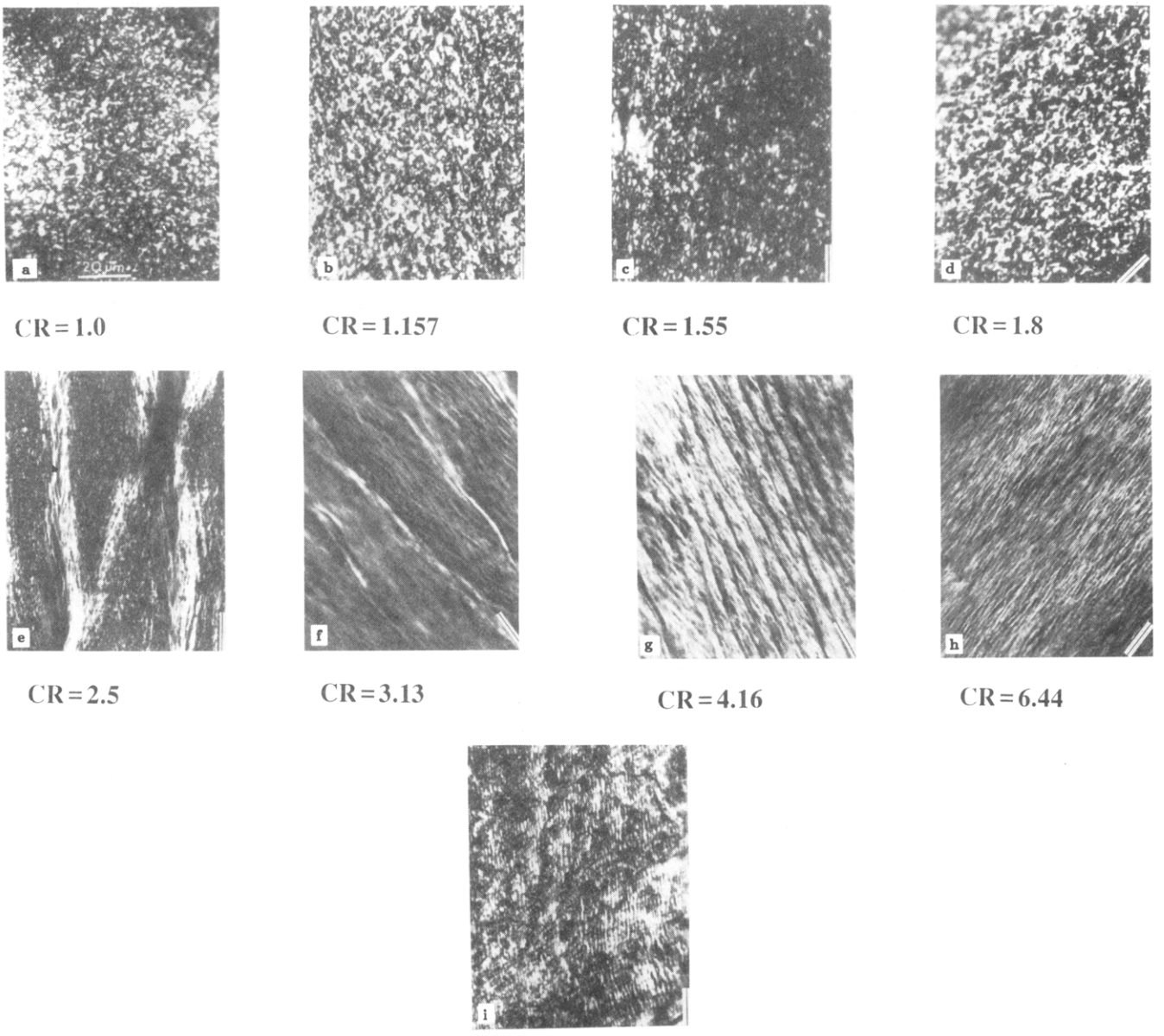


**Figure 3.** Polarizing light micrographs of linear polyethylene samples subjected to plane strain compression in a channel die to increasing compression ratios: (a) 1.0, (b) 1.157, (c) 1.55, (d) 1.8, (e) 2.5, (f) 3.13, (g) 4.16, (h) 6.44, and (i) 12.1. The lines in the lower right corners represent the flow direction. All viewing is in the constraint direction.

parallel to the flow direction. However, at a compression ratio of 3.13 most of thin lamellae undergo severe fragmentation. In ultrathin sections of those samples the lamellae are cut at preferred angles as it follows from their orientation and alignment due to plane strain compression. Hence, most of the cut lamellae are seen in the "edge-on" position. The coexistence of thin lamellae (120 Å, including adjacent amorphous layer) with thick areas (250 Å, including adjacent amorphous layer) in the same portion of ultrathin section is noticed (compare Figure 4e). Thick lamellae are mostly perpendicular to thin ones. At higher compression ratios fewer and fewer thick lamellae are observed. The lamellar fragmentation is better seen in the highly magnified micrograph of Figure 4h, which shows another portion of an ultrathin section sliced perpendicular to the constraint direction. At higher compression ratios these fragments rearrange and reorganize themselves to form new lamellae which are now oriented at an acute angle around the load direction (compare Figure 4f for compression ratio 6.0 and Figure 4g for compression ratio 6.44). These new lamellae are also extensively fragmented; the staining agent has penetrated lamellae in many places forming a grainy appearance. A complete interpretation of these important observations will be presented in section IV below.

**3.3. Small-Angle X-ray Scattering Results.** Small-angle X-ray scattering (SAXS) patterns shown in Figure 5 for undeformed and deformed samples were obtained including views in the three orthogonal directions associated with the channel die compression. The scattering pattern for the undeformed sample exhibits a well-defined isotropic ring, which indicates the presence in the sample of well-developed and randomly distributed lamellae. We must note, however, that the spacings of the long period estimated on the basis of the SAXS pattern are substantially higher than those estimated on the basis of TEM micrographs, reported in the previous section. The probable reason of that may be that scattering methods give a value which is a high-order average, favoring the largest objects in the specimen.

The patterns obtained for the samples compressed up to a compression ratio of 2.5 elongate with increasing compression, assuming oval shapes. The accompanying changes in the long period of lamella and amorphous

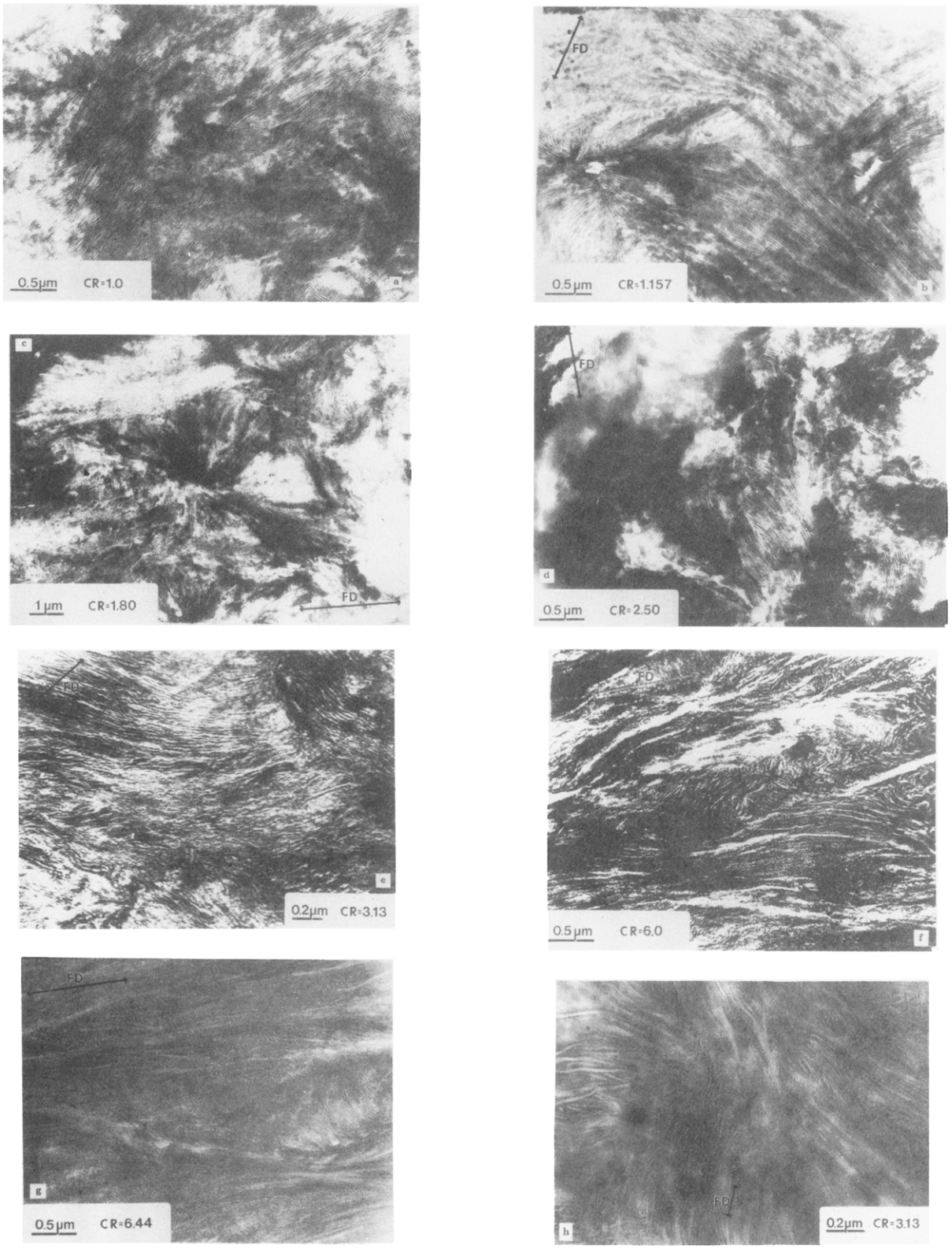


**Figure 4.** Electron micrographs of ultrathin sections of linear polyethylene subjected to plane strain compression. Sample planes are all normal to the constraint direction. The values of compression ratios are given in the micrographs as well as the direction of principal extension. Figure 4h is a magnified electron micrograph of an ultrathin section of linear polyethylene subjected to plane strain compression to a compression ratio of 3.13 showing fragmentation of lamellae and rotation of lameallar fragments in the opposite sense due to "coarse" chain slip.

layered elements oriented with their normals parallel to the principal directions, estimated on the basis of the SAXS patterns, are illustrated in Figure 6. The continuous decrease of the long period along the load direction is most probably due to chain slip in the lamellae.

In the sample with compression ratio 1.34 the SAXS patterns reveal some clustering of thinning lamellae along the flow direction (i.e., their normals along constraint direction). As the compression ratio increases to 1.55, 1.80, and 2.50, there is further clustering of lamellar orientations along the flow direction. The SAXS patterns for the sample compressed to the ratio 2.5 show that, among these lamellae oriented with their planes along the flow direction, the orientation with the lamella normals perpendicular to the loading direction is preferred. The progressive thinning of the lamellae is confirmed by the SAXS patterns

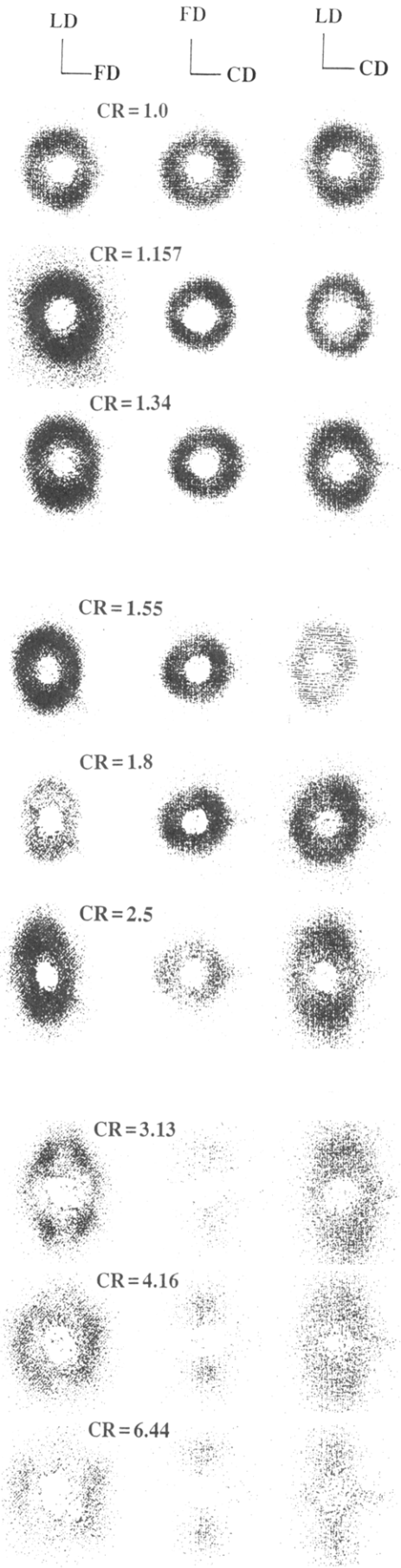


**Figure 5.** Small-angle X-ray scattering patterns of polyethylene samples subjected to plain strain compression. The direction of the incident X-ray beam is along the constraint direction; the load direction or the flow direction; compression ratios are 1.0, 1.157, 1.34, 1.55, 1.8, 2.5, 3.13, 4.16, and 6.44, respectively.

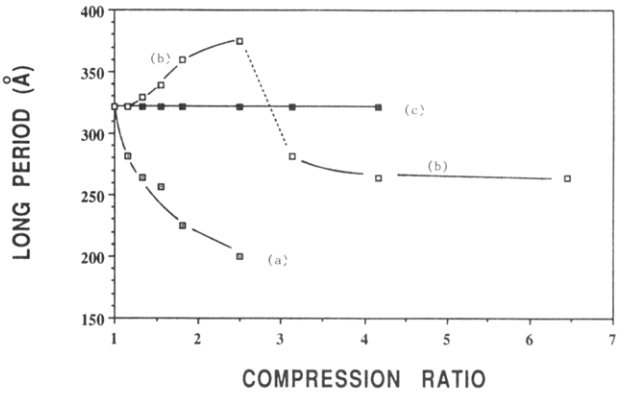


**Figure 6.** Dependences of the long period, determined by SAXS, in the particular direction on the same deformation: (a) long period along the loading direction; (b) long period along the flow direction; (c) long period along the constraint direction.

recorded while the samples are viewed along the constraint direction and along the flow direction.

New features appear clearly at a compression ratio of 3.13: the SAXS pattern for the constraint direction view becomes a new four-point pattern; the pattern obtained by viewing in the load direction resembles a two-point image; the pattern recorded by viewing in the flow direction shows further clustering of orientation of scattering elements with their normals parallel to the load direction. The outline of the four-point pattern observed along the constraint direction could be already recognized at a compression ratio of 2.5, although it was not yet as well developed as in the sample compressed to the compression ratio 3.13. Moreover, the change of the shape of the SAXS pattern recorded along the loading direction, from elliptical to the two-point type, is accompanied by the abrupt decrease of the long period along the flow direction (see Figure 6). The intensity of the scattering by the sample compressed to the ratio 3.13 viewed in the loading direction, as well as viewed in the flow direction, is very weak and increases gradually with further deformation. This may suggest that at compression ratio 3.13 the population of lamellar crystallites oriented with their normals parallel to the flow direction is relatively small, whereas lamellae oriented with normals along the constraint direction almost disappear (changing their orientation), or that the periodic arrangement of the crystals was substantially disturbed at this stage of deformation and was subsequently improved with increasing deformation. As the compression ratio is increased, first to 4.16 and then to 6.44, the four-point pattern for the constraint direction view transforms into two arcs, now normal to the flow direction. The two-point pattern for the loading direction view is now much better outlined, indicating the complete elimination of lamellae oriented with their normals parallel to the constraint direction. The clustering of orientations viewed in the flow direction transforms gradually into a weak and diffuse two-point pattern. These data show that the long-period planes were oriented first preferentially perpendicular to the load direction and then, above a compression ratio of about 2.50 the SAXS patterns recorded along the flow direction become progressively fainter showing a gradual elimination of that long period, i.e., lamellae oriented previously with their normals parallel to the loading direction. The meaning of these observations in the context of TEM results will also be discussed in section IV below.

**3.4. Wide-Angle X-ray Scattering Results.** Pole figures of molded specimens not subject to channel die compression were featureless, confirming the isotropy of the molded specimens observed at a different level with

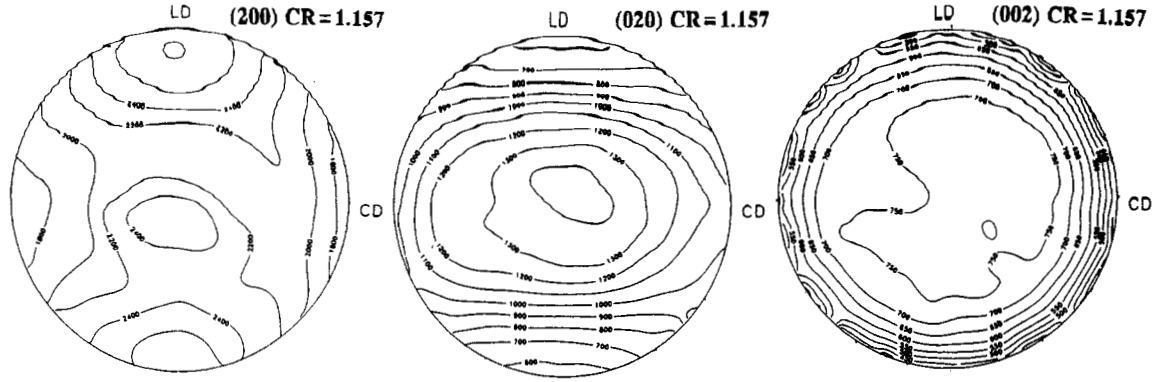


**Figure 7.** Pole figures of normals to the (a) (200), (b) (020), and (c) (002) planes of orthorhombic crystals of linear polyethylene subjected to plane strain compression. Compression ratio 1.157.

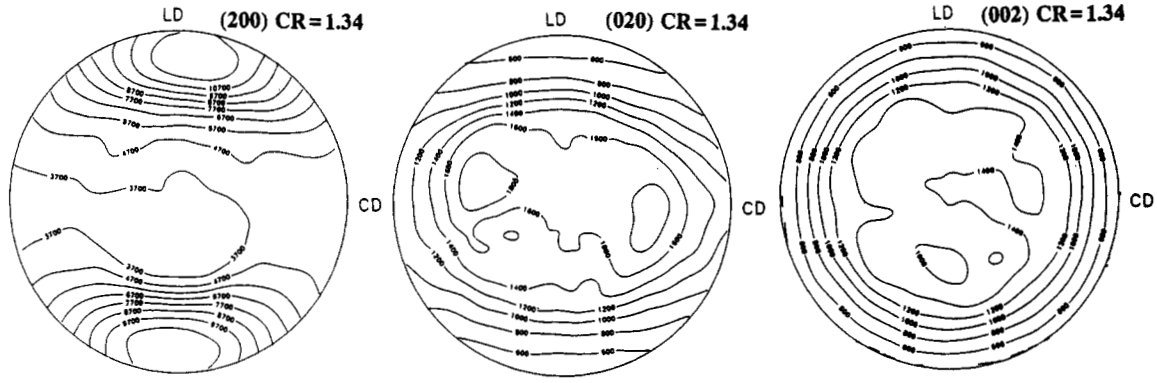


**Figure 8.** Pole figures of normals to the (a) (200), (b) (020), and (c) (002) planes of orthorhombic crystals of linear polyethylene subjected to plane strain compression. Compression ratio 1.34.

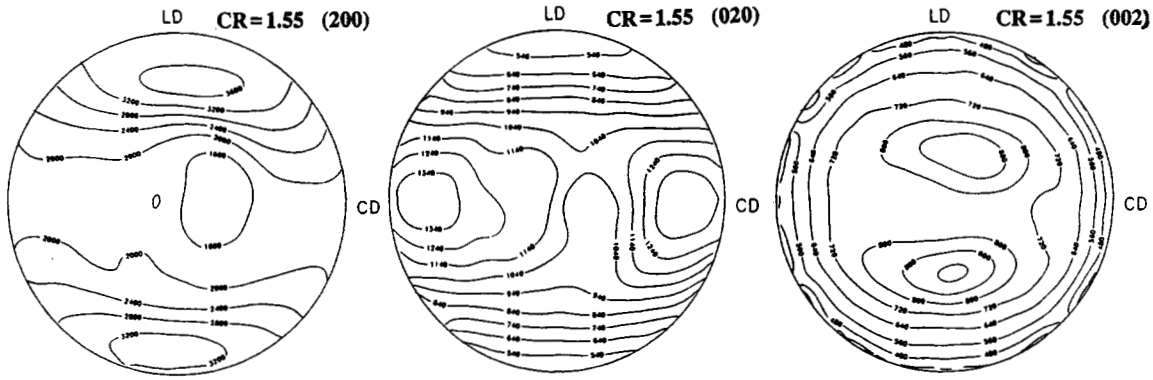


**Figure 9.** Pole figures of normals to the (a) (200), (b) (020), and (c) (002) planes of orthorhombic crystals of linear polyethylene subjected to plane strain compression. Compression ratio 1.55.

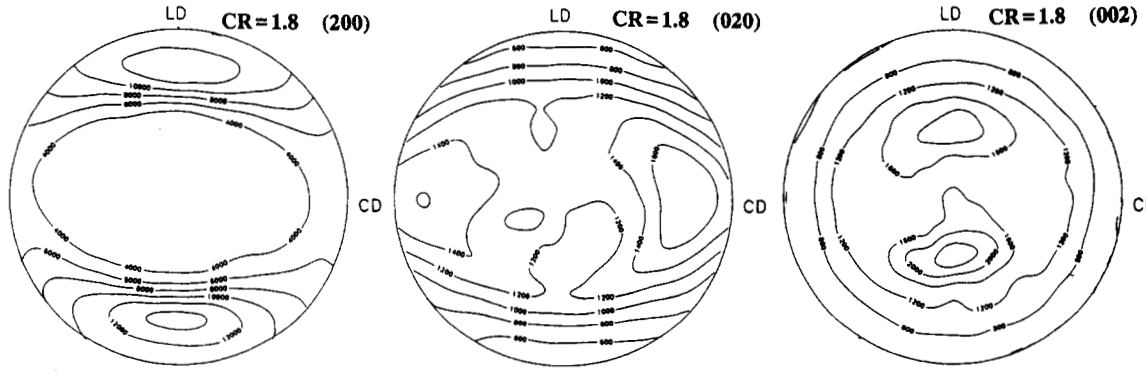


**Figure 10.** Pole figures of normals to the (a) (200), (b) (020), and (c) (002) planes of orthorhombic crystals of linear polyethylene subjected to plane strain compression. Compression ratio 1.8.

optical microscopy and SAXS experiments described above. In Figures 7a–c to 15a–c pole figures of normals to the (200), (020), and (002) planes for samples with compression ratios of 1.16, 1.34, 1.55, 1.80, 2.50, 3.13, 4.16, 6.44 and 12.1 are depicted, all viewed in the flow direction. Since lattice rotation is the process which results in preferred orientation of the deformed material in response to a variety of crystallographic slip processes and interlamellar sliding by shear of the amorphous material, we have constructed schemes of rotations of crystal fragments due to two of the possible slip operations and interlamellar sliding. These are illustrated in Figure 16. In Figure 16a the rotations that are associated with (100)[001] chain slip and its counterpart of interlamellar sliding is depicted,

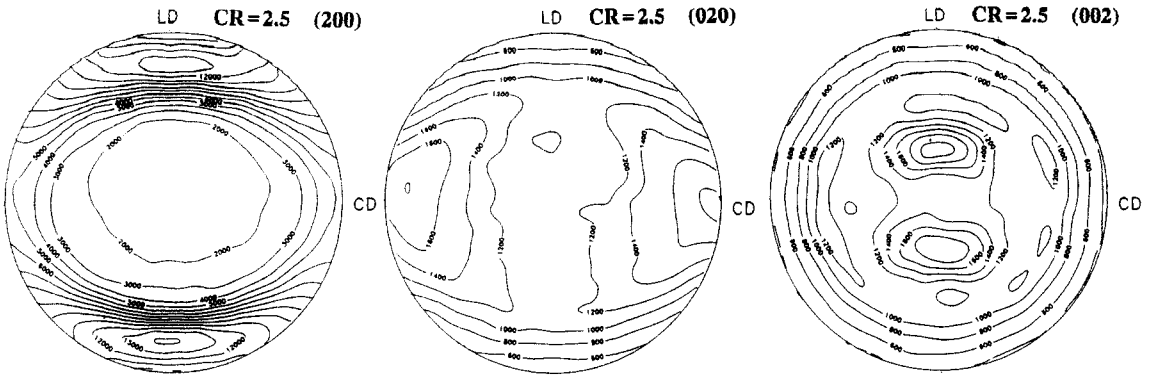


**Figure 11.** Pole figures of normals to the (a) (200), (b) (020), and (c) (002) planes of orthorhombic crystals of linear polyethylene subjected to plane strain compression. Compression ratio 2.5.

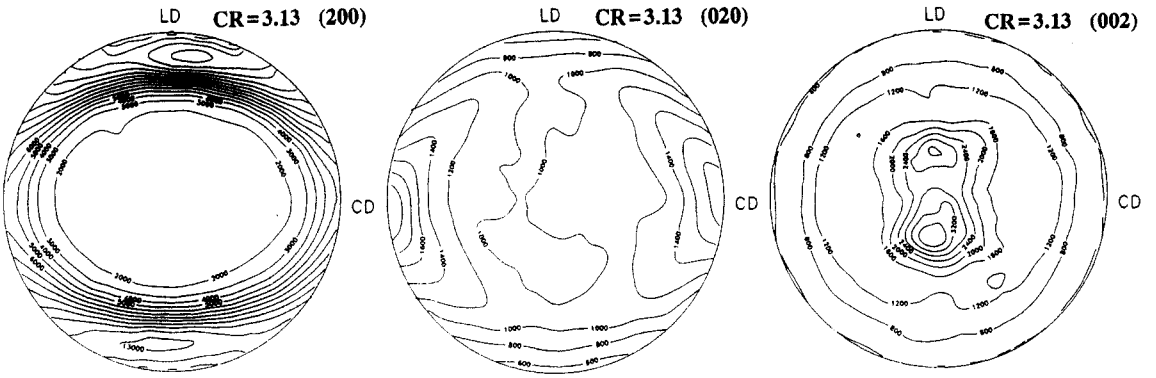


**Figure 12.** Pole figures of normals to the (a) (200), (b) (020), and (c) (002) planes of orthorhombic crystals of linear polyethylene subjected to plane strain compression. Compression ratio 3.13.

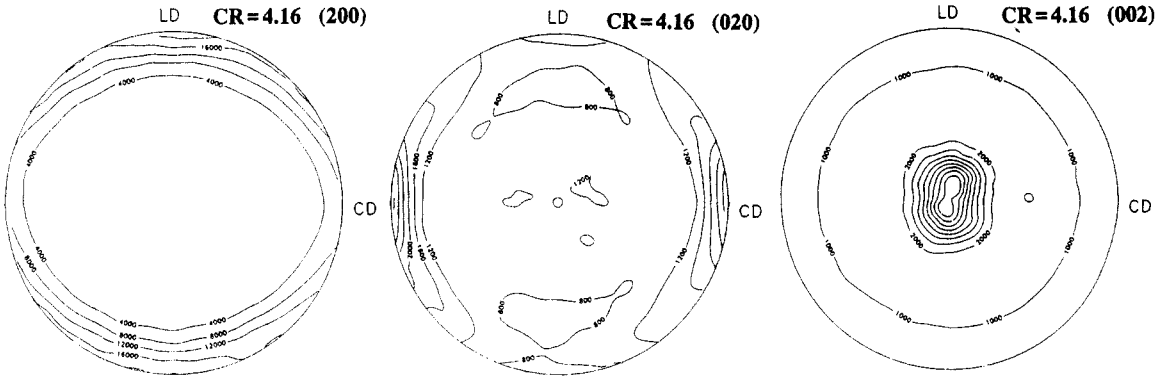


**Figure 13.** Pole figures of normals to the (a) (200), (b) (020), and (c) (002) planes of orthorhombic crystals of linear polyethylene subjected to plane strain compression. Compression ratio 4.16.

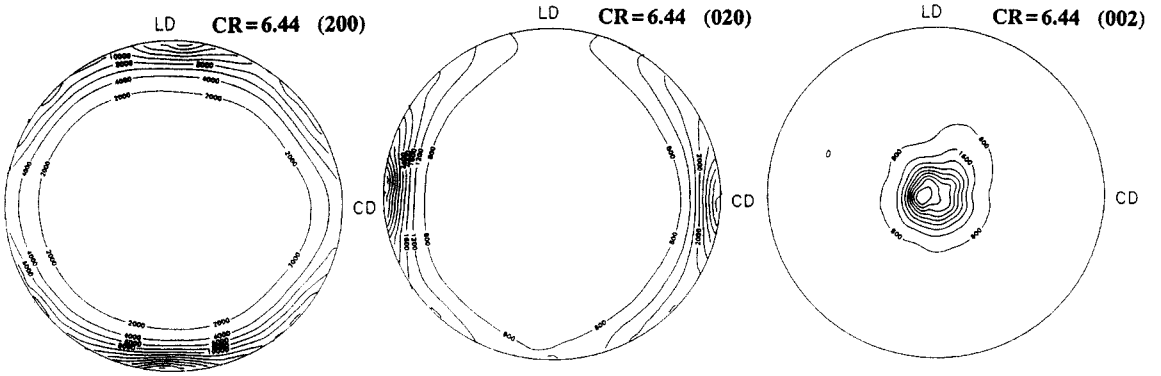


**Figure 14.** Pole figures of normals to the (a) (200), (b) (020), and (c) (002) planes of orthorhombic crystals of linear polyethylene subjected to plane strain compression. Compression ratio 6.44.

while Figure 16b gives the rotations that are associated with (010)[001] chain slip and its counterpart of interlamellar sliding. The most important observation from these schemes is that the crystallites rotate due to interlamellar sliding in the opposite direction from that due to crystallographic slip. Similar schemes may also be constructed for other slip systems. In bulk samples the load is applied in the loading direction and the initial orientation of crystals is random. The rotations associated with interlamellar sliding, crystallographic slips, and twinning introduce preferred orientation of crystallites. If chain slip on the (100)[001] slip system was the only

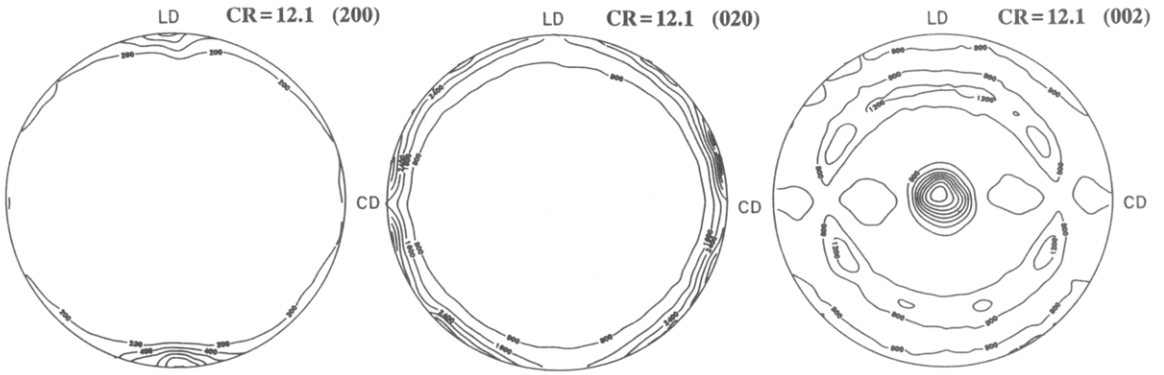


**Figure 15.** Pole figures of normals to the (a) (200), (b) (020), and (c) (002) planes of orthorhombic crystals of linear polyethylene subjected to plane strain compression. Compression ratio 12.1.

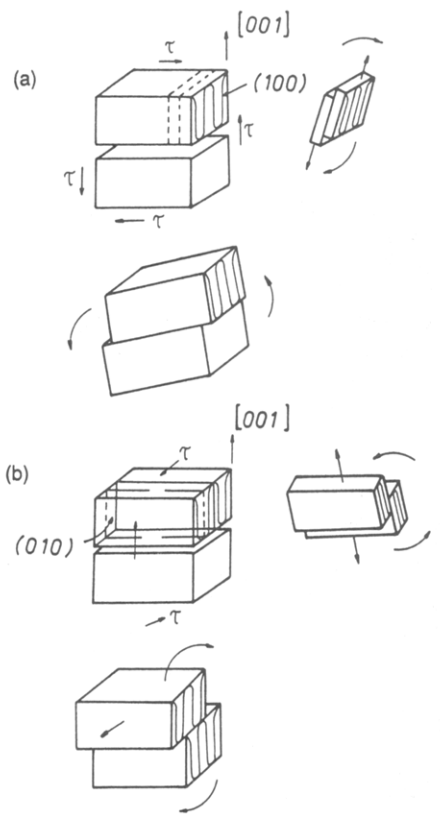


**Figure 16.** Sketch of rotations that result from two separate mechanisms of chain slip ((100)[001] and (010)[001]), and the associated interlamellar sliding.

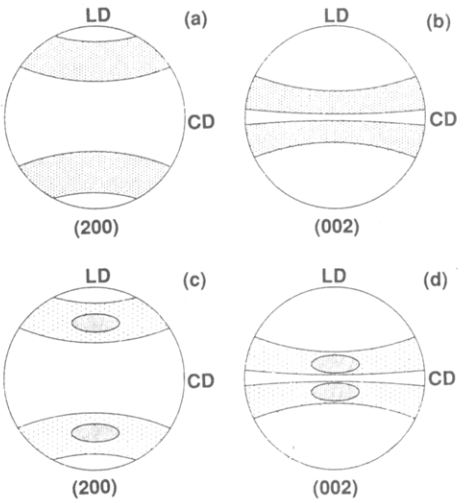


**Figure 17.** Predicted textures that result from (100)[001] chain slip and accompanying rotations imposed by compression from the LD direction; (a) and (b) deformation without constraints; (c) and (d) constraints in the CD direction.

mechanism of deformation and if there were no constraints, then the pole figures that would arise from the lattice rotations due to the deforming crystallites can be readily predicted and are shown in Figure 17a,b. It may be expected that the constraints imposed in the constraint direction during deformation will restrict to some extent the rotations of crystallites in the plane perpendicular to the flow direction. The expected pole figures for that case are presented in Figure 17c,d.

Parts a–c of Figure 7 present the pole figures of normals to the (200), (020), and (002) planes of the orthorhombic structure of initially spherulitic polyethylene, deformed to a compression ratio of 1.16. It is seen that the normals begin to exhibit a certain degree of orientation. Comparison of these pole figures with the predicted ones presented in Figure 17 leads to the conclusion that the (100)[001] chain slip system, associated with the rotation of chain segments in the lamellae, is responsible for such a pattern of orientation. Lateral constraints are not yet affecting the rotations significantly. The small but pronounced peak in the center of the pole figure for normals to the (200) planes either is the result of interlamellar sliding which could have occurred at a lower compression ratio and, upon being locked, was subsequently superceded by (100)[001] chain slip or, less probably, is due to residual (200) planes from the initial undeformed orientation distribution.

At a compression ratio of 1.34 (see Figure 8a–c) the evidence for further (100)[001] chain slip and the associated chain segment rotation in the load direction–flow direction plane is more pronounced. In Figure 8b where the pole figure of (020) normals is presented there is clear evidence of rotation of the normals to the (020) planes in the constraint direction–flow direction plane toward the constraint direction. Such a rotation could be induced either by (100)[001] chain slip in the presence of strong constraints in the constraint direction or rather by the simultaneous activity of two slip systems: (100)[001] chain slip and (100)[010] transverse slip cooperating in the (100) plane. The (010)[001] and (110)[001] chain slip systems as well as martensitic transformations and twinning modes are evidently still largely inactive. In the (002) pole figure (Figure 8c) the (002) plane normals now show a clear preference to clustering toward the flow direction.

At a compression ratio of 1.55 the (100)[001] chain slip, (100)[010] transverse slip, and their associated rotations may be still recognized, as can be seen in Figure 9b,c. Figure 9c shows clearly that the (002) normals, i.e., the axes of the chain in the lamellae, continue to cluster close to the flow direction, which is expected for (100)[001] chain slip. The confirmation of the rotation due to (100)[010] transverse slip can be found in Figure 9b where the maxima

of orientation of the (020) normals shift clearly toward the constraint direction, as is expected for simultaneous activity of (100)[010] and (100)[001] slips and accompanying rotations. However, in Figure 9a, showing the pole figure for normals to the (200) planes, the distribution of orientations of these normals become somewhat broader and, moreover, shift slightly away from the loading direction, which is a rotation in an opposite direction than expected on the basis of postulated slip systems. We observed identical behavior in polyethylene deformed in uniaxial compression in the same strain range and found that the reason of this unexpected rotation of the poles of the (200) planes and broadening of their distribution is the "locking" of lamellar sliding, which is partially reversible on unloading at relatively low strains and becomes irreversible only at higher strains.[22]

At a compression ratio of 1.8 (Figure 10a–c) and 2.5 (Figure 11a–c) plastic deformation occurs via two cooperative slip processes, (100)[001] and (100)[010], as discussed earlier. There is still little evidence for activity on the (010)[001] chain slip system.

The patterns of pole figures for the sample with compression ratio 3.13 are depicted in Figure 12a–c. These figures now present evidence of intense accumulated activity on the (100)[001] and (100)[010] cooperative slip systems. The (010)[001] chain slip showed little activity up to this stage of deformation, as is evident from the lack of movement of the concentrations of (010) normals toward the loading direction in Figure 11b. This could in large part be a result of the already well-developed clustering of the (010) plane normals parallel to the constraint direction due to the intense previous cooperative activity of the (100)[001] and (100)[010] slip systems, which probably masks any change of orientation distributions due to weaker activity of other slip systems. It can be concluded that the intense shear bands observed in the polarizing light microscope in the samples deformed to this compression ratio are mainly due to the most prevalent (100)[001] chain slip system.

The pole figures for the sample with compression ratio 4.16 are presented in Figure 13a–c. Evidence of continued very intense (100)[001] chain slip and intense (100)[010] transverse slip is present. The chain segments in crystals are now aligned almost completely parallel to the flow direction due to intense chain slip, inducing the rotations of chain segments toward the flow direction. The pole figures for the sample with a compression ratio of 6.44 are shown in Figure 14a–c. The deformation, predominantly by (100)[001] chain slip, but secondarily by (100)[010] transverse slip, and perhaps also by (010)[001] chain slip have finally resulted in a high degree of orientation of crystals, producing a texture resembling a monocrystal.

Further deformation of this monocrystal texture to a compression ratio of 12.1 must occur by still active chain slips: (100)[001] and (010)[001]. The small fraction of crystals which at the compression ratio of 6.44 was still oriented with their (200) normals between the load and constraint directions has now become substantially parallel to the load direction, apparently primarily by rotation due to (100)[010] transverse slip activity (see Figure 15a). Evidence of some fibrillar texture instead of the monocrystal texture is seen in Figure 15b, showing a somewhat reduced concentration of (020) poles in the constraint direction. Twinning processes could be responsible for this trend to fibrillar texture.

Because of partial overlapping of (110) and (200) peaks together with the amorphous halo and the reflections from the monoclinic modification in the diffraction patterns, the deconvolution of X-ray peaks for the purpose of constructing clearer pole figures was performed for X-ray

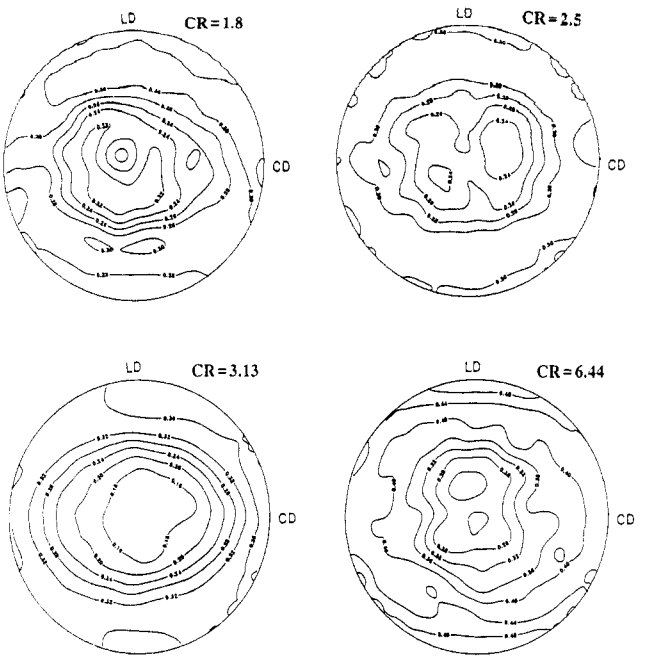


**Figure 18.** Deconvoluted pole figures of the (200) peak width for samples with the following compression ratios: (a) 1.8; (b) 2.5; (c) 3.13; (d) 6.44.

data collected for samples which were compressed to the following deformation ratios: 1.80, 2.50, 3.13, and 6.44. In Figure 18a–d the postdeconvolution "pole figures" constructed for (200) peak width are presented for these samples. These figures are the maps in crystallographic projection of the half-width of the deconvoluted (200) diffraction peaks given by crystallites oriented with their (200) planes in the way defined by the map coordinates. Because peak width depends primarily upon the size of the crystal in the direction perpendicular to the diffracting plane, the constructed map may be interpreted in terms of the size of specifically oriented crystallites.[18,20] The (200) X-ray reflection becomes broader for those orientations where the (200) normals are concentrated (see Figure 10a, 11a, 12a, and 14a for corresponding fractions of crystallites). For the sample with a compression ratio of 6.44 the peak width for those orientations along which most crystallites are aligned is twice the peak width for undeformed material. This is an additional indication of intense (100)[001] slip driving the entire deformation process and the systematic reduction of the average dimension of the diffracting crystallites.

Parts a–d of Figure 19 show pole figures constructed from the integrated intensity of the amorphous halo, for compression ratios 1.80, 2.50, 3.13, and 6.44, respectively. The amorphous halo appearing in the $2\theta$ range 16–25° contains largely intermolecular information. The interpretation of the amorphous diffraction pattern is possible if the packing of neighboring macromolecules is modeled. Assuming a two-dimensional pseudohexagonal close packing of molecules, the amorphous halo produces reflection in the (100) range. Hence, the construction of pole figures for the total amorphous halo intensity and half-width provide information about the orientation of normals to fragments of macromolecular chains in the amorphous regions, and about the size of these "ordered" regions.[18–20] From Figure 19a–d it is seen that the chains in the amorphous phase assume an orientation parallel to the flow direction. There are also two, not very distinct, maxima of orientations emerging that are tilted at some acute angle with respect to the flow direction. As the compression ratio increases, the orientation of the chains in the amorphous phase tending toward the flow direction

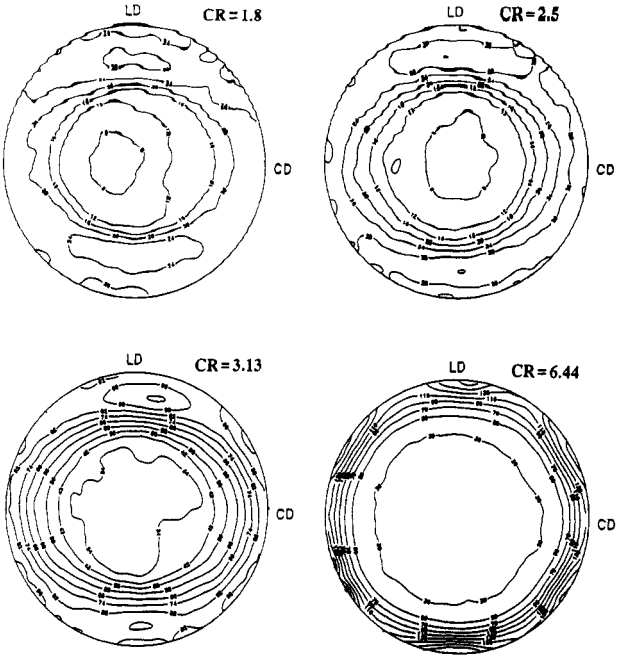


**Figure 19.** Deconvoluted pole figures of integrated intensity of the amorphous halo for samples with the following compression ratios: (a) 1.8; (b) 2.5; (c) 3.13; (d) 6.44.

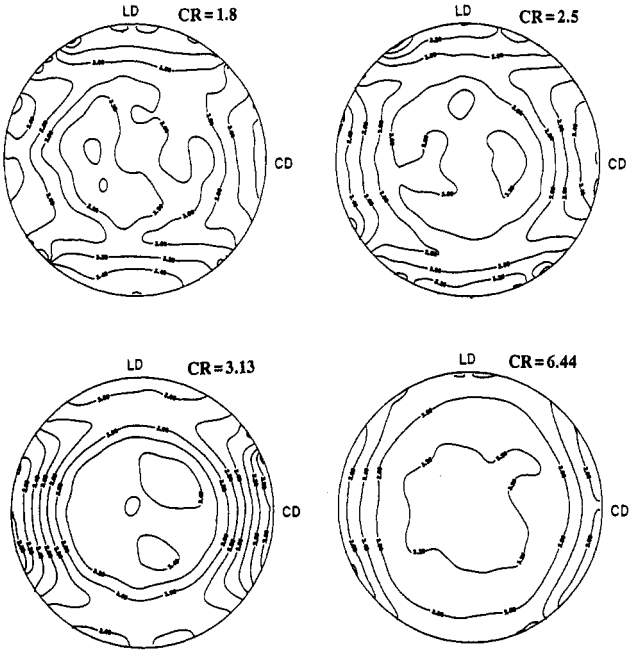


**Figure 20.** Deconvoluted pole figures of the amorphous peak width for samples with the following compression ratios: (a) 1.8; (b) 2.5; (c) 3.13; (d) 6.44.

becomes more and more pronounced. In Figure 20a–d the pole figures for amorphous peak half-width are depicted for samples deformed to compression ratios of 1.80, 2.50, 31.3, and 6.44, respectively. These pole figures for peak widths indicate that the amorphous peak sharpens as the compression ratio increases. At a compression ratio of 6.44 almost all amorphous material is quasi-close-packed in the sense of regularity of intermolecular distance, as Figure 19a–d for the corresponding fractions of the amorphous phase shows. In interpreting this information on alignment of molecular segments in the amorphous material and the meaning of the half-widths of the amorphous halo, we must recall that the amorphous material is tied to the crystalline material and that improved texturing of the amorphous material does not necessarily imply deformation activity in that material.

Figure 21 presents the results of measurements of the

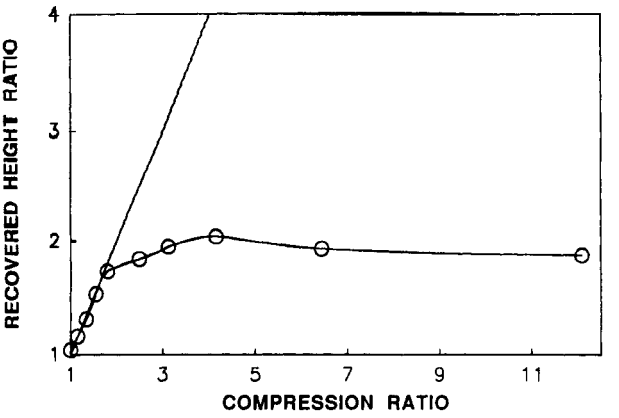


**Figure 21.** Recovery of the width during temperature rise up to the melting point with a heating rate of 10 °C/min of samples subjected to plane strain compression.

expansion in the load direction due to thermal relaxation for compressed polyethylene samples, upon unloading and raising the temperature close to the melting point. Clearly, this expansion is substantial and restores the sample to almost the initial size, for compression ratios of up to 1.80. For further compression the recovery is progressively less complete, and the deformation is increasingly more permanent. Above a compression ratio of 4.16 the total amount of recovery becomes even less than that for lower compression ratios. It can be concluded from these observations that up to the compression ratio of 1.8, the deformation is substantially affine and, on the molecular scale, does not induce any significant change of the end-to-end distance of the molecules, which "remember" their initial shape. Above a compression ratio of 1.8 the deformation becomes kinematically irreversible as a result of the intense slip. Above a compression ratio of 4.16 it appears that some scission of chains occurs, so the total amount of recovery is somewhat smaller.

## IV. Discussion

We have presented results on changes in density and morphology, the latter observed by polarized light microscopy and X-ray diffraction, including diffraction peak deconvolution results via pole figures; all of these observations are useful for probing the developing texture of high-density polyethylene during plane strain compression in a channel die. The results convey much information on the mechanisms of deformation during such large compression. On the basis of the WAXS and SAXS studies the most active slip mechanism in all of this deformation is (100)[001] chain slip. The other slip processes that have been recognized are (100)[010] transverse slip, perhaps (010)[001] chain slip, and some twinning that comes in the very late stages. Interlamellar sliding is observed unambiguously only in the initial stages of deformation, before (100)[001] chain slip sets in. While there is no clear evidence for continued activity of interlamellar sliding, its presence in later stages of deformation cannot be ruled out entirely for clear kinematic reasons.

Nevertheless, the existing evidence suggests that interlamellar sliding is exhausted in the early stages of deformation, probably near a compression ratio of 1.55, and the interlamellar amorphous material "locks" after being stretched out. At a compression ratio of 1.8 (100)-[010] transverse slip is seen to become active. At a compression ratio of 3.13 (010)[001] chain slip probably becomes active, too. The activation of (100)[010] transverse slip is responsible for most of the final perfection of the near-monocrystal texture, particularly in rotating the

(010) plane normals parallel to the constraint direction. The onset of twinning at the highest compression ratios causes the partial deterioration of the almost perfect monocrystal texture by rotating some of the (010) plane normals away from the constraint direction. Our study has clarified a number of additional important points that have not been appreciated previously.

First, as already stated above, while deformation in the amorphous interlamellar material is the easiest to initiate in PE and is clearly observable in the pole figures of compression ratio of 1.157, it is expected to "lock" in monotonic shear once the amorphous material achieves its limiting molecular extension ratio. It is expected, however, that such locking will depend on molecular weight characteristics and sample thermal history. Beyond this limiting extension ratio, the amorphous material should contribute little to further monotonic deformation, short of becoming available again in reverse deformation, or upon large rotation of the surrounding crystallites.

Second, by virtue of the large superimposed pressure component during the deformation, there is no significant internal cavitation of the type noted in tension experiments by the early investigators that has been referred to as "micro-necking" by Peterlin (see e.g. ref 4). Such "micro-necking" had been considered for a long time to be essential for large strain deformation of aggregates of chain-folded crystallites, where it was thought to remove kinematical constraints between the lamellae and permit them to unravel. While this scenario could still be partially correct in tensile deformation, our experiments have shown that it is inessential for the development of the nearly perfect textures that result from plane strain compression. Our, WAXS, SAXS, TEM, and light microscopy observations presented in section III above indicate convincingly that although much inhomogeneous deformation in the form of shear localization occurs during deformation, locally the material elements, consisting of aligned chain lamellae and associated amorphous regions, undergo a continuous series of shear-induced morphological transformations—without any intervening cavitational process. The density reductions that have been noted in Figure 2a,b are apparently quasi-homogeneously dispersed processes of little primary consequence. Their nature could not be identified directly. As is discussed by Bartczak et al.,[6] in a related study, however, some observed shear resistance anomalies in the fully textured material would appear to be related to such diffuse local decohesion.

The absence of a complex cavitational process during deformation permits the successful simulation in the computer of texture-forming large strain deformation by a continuous series of shear transformations of space-filling aggregates of adjoining chain-fold crystalline lamellae and amorphous regions; such simulations are presented in another related study of Lee et al.[15] As we will discuss below, however, a lamellar fragmentation process, that intervenes in the range of compression ratio of CR = 3.13, introduces a major restructuring of morphology without cavitation that must be incorporated explicitly with the above-mentioned simulations.[15]

Third, our TEM and SAXS studies show that the initial interlamellar amorphous material, attached to the lamellae, and apparently in fully sheared and locked form, is carried along with the crystalline lamellae as the latter undergo chain slip and rotation. As a result these amorphous material layers become oriented nearly perpendicular to the loading direction, and thus parallel to the (100) planes of the stretched lamellar crystals. This is evident from the SAXS patterns viewing the deformation from the flow direction, as shown in Figure 5, and is also clearly seen in the TEM micrographs of Figure 4d–f. This orientation of the amorphous material layers is predicted faithfully by the associated computer simulation of Lee et al.[15] As is well-known, however, the long period in the final fully textured material is nearly perpendicular to the flow direction or the direction of principal molecular alignment. The formation of this new long period, as a major morphological restructuring process, had never been fully elucidated in the past. In the present study its formation was clearly discernable in the SAXS patterns starting with a compression ratio of 3.13 and became progressively better defined with continued deformation. The evoluation of the new long period is better seen in the TEM micrographs of Figure 4e and particularly Figure 4f, starting with the widespread "fragmentation" of the stretched out lamellae, which we pointed out earlier in section 3.2 above. How this newly-evolving amorphous material may be topologically related to the initial amorphous material is one of our principal findings and is explained in detail below.

The TEM results clearly indicate that beginning at a compression ratio of 3.13, an intense fragmentation of lamellae is taking place. It is evident from Figure 4h, showing a high-magnification micrograph of an ultrathin section of the 3.13 sample, that these fragments of lamellae rotate in the direction away from the flow direction.

This rotation of lamellar fragments is opposite to the rotation resulting from fine-chain slip. This type of behavior of stretching out of the initial lamellae and carrying the interspersed amorphous material with it, followed by their fragmentation, was reported first by Young et al.[23] They have attributed the development to a so-called "coarse chain slip" in subsequent deformation, that fragments the stretched lamellae by (100)[001] chain slip occurring in coarse steps. While this scenario appears to fit the observations at first sight, such profuse shearing is not favored in the already highly aligned chains of the lamellae producing the large block-like motions by deformation-induced processes since the resolution of shear stress (Schmid factor) along the (100)[001] system due to the applied stresses, or imposed deformations, should have decreased to quite low values. Therefore, we propose a different explanation for these observations, that is more consistent with expectations of decreasing Schmid factors, and recognizing other important thermodynamic driving forces related to structural rearrangements of a topological nature and not associated with strain production. This suggested alternative development is pictorially outlined in Figure 22.

In Figure 22a a typical domain of lamellae and associated amorphous regions of the initial, melt-solidified, structure is shown in relation to the loading direction (LD) and the flow direction (FD) of the deformation that is to be imposed on it. As the imposed deformation proceeds, the lamellae undergo shear on the most prominent chain slip system of (100)[001]. As shown schematically in Figure 22b, the lamellae, as a result, stretch out, become thinner, and undergo a lattice rotation tending to align the molecules and the planes of the associated amorphous regions in the FD direction; i.e., molecules align and rotate toward FD while the normals to the (100) planes and the planes of the amorphous material rotate into the LD direction. This process continues monotonically through the compression ratio of 2.5 (Figure 22c) until a compression ratio around 3.13 is reached, where the lamellae now have become quite elongated and on the average have thinned down to one-third of their initial thickness. The associated amorphous region, while no longer responding independently, is forced to go along with the shearing and thinning lamellae. On the basis of the observations reported in section III, it is postulated that the continued monotonic thinning of the

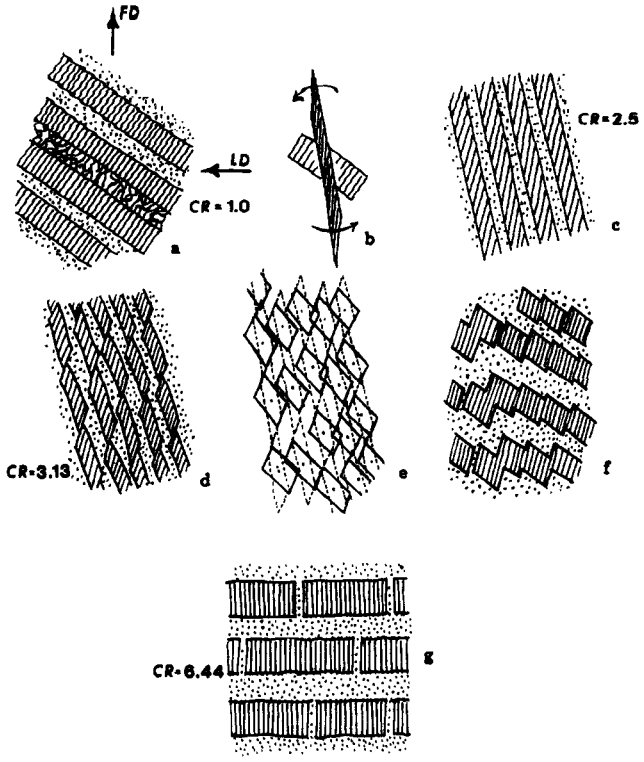


**Figure 22.** Sketch of the process of the formation of a "new" long period due to a plane strain compression.

lamellae by chain slip becomes unstable—much like the continued elongational thinning of a layered heterogeneous fluid becomes unstable and responds by periodic pinching off. In structureless fluids the principal stimulus for such pinching-off and breakup of the stacks of layers is the instability of the ever increasing interface energy to perturbations of certain wavelength. In the present case of the stretching lamellae and their amorphous layers this interface instability should also be present while the required perturbations should come from thickness irregularities and other plastic resistance inhomogeneities present in all cases of crystal plasticity. While the perturbation problem of the initiation and growth of a deformation instability involving a stretching interface between a component deforming by crystal plasticity and another amorphous component deforming by a less well understood mechanism is a major undertaking, estimation of the conditions of its onset is easier. In the plane strain stretching of a layered plastic medium of two components with plastic shear resistances, $\tau_c$ (crystalline) and $\tau_a$ (amorphous), the interface stretching resistance should contribute little to the overall resistance when the scale $\lambda$ for the problem (here the long-period wavelength) is large. When this dimension becomes very small, however, the interface-stretching resistance becomes comparable with the plastic-stretching resistance of the crystalline and amorphous layers, and perturbations decreasing the overall interface energy are likely to grow. An elementary plane strain stretching analysis (see Appendix I) gives this dimension $\lambda$ where the two resistances become equal as

$$\lambda = \frac{\chi}{(c\tau_c + (1-c)\tau_a)} \tag{1}$$

where $\chi$ is the interface energy and $c$ the volume fraction of the crystalline component. For an order of magnitude estimate, we take $\chi = 0.093$ J/m$^2$,[24] and $\tau_c = 7.2$ MPa[6] and guess $\tau_a$ to be around 5 MPa;[15] for a volume fraction of crystallites of 0.5, this gives $\lambda = 15$ nm, which is in the right range of lamella thicknesses, where they are observed to break up (i.e., about 12 nm). The expression in eq 1 is not the result of a full model but merely a scaling argument, making it likely that our estimate lacks additional numerical terms of the order of $(0.5–2)\pi$. Second, the breakup could be hastened by plastic inhomogeneities or irregularities in the thickness of lamellae. This breakup of lamellae is depicted in Figure 22d. Once this process begins, the pinching-off of the lamellae could give rise to local strain softening and concentration of further deformation at coarser spacings. We propose that this is the origin of the so-called "coarse chain slip" process of Young and Bowden.[7]

The more important matter, however, is that once the lamellae are fragmented, the fragments can change shape (without producing any additional strain or giving rise to any additional lattice rotation or even rotate in the opposite direction) to reduce the interface energy. This should happen by the migration along the chains of the accumulated chain defects that make up the amorphous material. This purely topological reordering is depicted in Figure 22e as a virtual shape change exercise around the centers of the fragments of the lamellae. As depicted further in Figure 22f, such restructuring should give rise to a new long period where the new topologically distorted (without lattice shear of the crystalline lamellae) lamellar fragments touch and associate. Clearly, the sequence of events shown in Figure 22d–f is an idealization—all occurring at a compression ratio of 3.13. In reality such restructuring cannot be spontaneous throughout the entire structure but will continue over an increment of additional plane strain flow, eventually at CR 6.44, giving rise to the quasi-single crystalline morphology depicted in Figure 22g, where the plane of the new long period is now across the aligned chains.

Several important factors of this restructuring process are worthy of note. First, all of it can be accomplished without a catastrophic step of cavitation such as "micronecking" that had been thought to be necessary for full chain alignment. We recognize, however, that the deformation instability depicted in Figure 22d–f could give rise to cavitation in a tensile field which then could mask the true nature of the essentially continuous processes of deformation and the principal driving forces of interface energy reduction. Second, the scenario presented above shows in full detail how the old amorphous material layers that are initially stressed and rotated out of the way to lie in the FD–CD plane (plane normals parallel to LD) become gradually and continuously transformed into the amorphous fraction of the new long period constructed perpendicular to the aligned chains. Third, the development indicates that a vestigial fraction of the old amorphous material must remain behind in the form of chopped-up layers perpendicular to LD. This remaining amorphous material is, in all probability, responsible for the relatively easy delamination of the fully aligned quasi-single crystalline material. Fourth, since the amorphous fraction of the new long period is primarily constructed of chain defects (tie links, etc.) that have good mobility along the chain, it is useful to think of the fully textured quasi-crystal as having a continuous background of crystal with layers of segreated chain defects making up the new long period. In this sense an analogy to the morphology of heavily deformed metal single crystals having nearly perfect crystalline cells, separated by regularly spaced cell walls, made up of dense collections of crystal dislocations should prove to be very useful in interpreting the plastic shear response of the new quasi-crystal in the FD direction.

The model of restructuring of morphology that we have outlined explains the zigzag pattern of the new lamellae when the sample is viewed along the constraint direction. This was first noted in the study of Song et al.[17] The length of the zigzags is correlated with the thickness of

stacks of lamellae in the original undeformed material. The thicknesses of the new lamellae are determined by the thickness of the lameallae in the initial unoriented material and by the critical tilt angle of the chain axes with respect to the lamellar surface at which the stretching of the lamellae becomes unstable and "coarse" chain slip becomes activated. The last factor is likely to be fairly sensitive to the temperature and strain rate. The chain axis orientation is retained in the new lamellae, as should be clear from Figure 22.

Finally, the observations reported here on the kinematics and the resulting stress–strain behavior of the deforming assembly of lamellae and their associated amorphous regions are fully consistent with a detailed computer model of the deformation (excluding the important lamellar restructuring process discussed here) that is presented in a companion study by Lee et al.[15] elsewhere.

## Appendix I

**Plane Strain Compression of a Stack of Lamellae and Associated Amorphous Material.** Figure A1 shows a sketch of alternating crystalline lamellae and associated sheets of amorphous material in a state of extensional flow as would be the case in channel-die compression. We neglect elastic response but consider both the crystalline lamellae and the amorphous material to deform in a rigid-plastic manner in the $x-y$ (LD–FD) plane. The principal periodicity of the structure is $\lambda$, which is the so-called long-period wavelength. The tensile plastic resistances and volume fractions of the crystalline and amorphous components are $Y_c, Y_a$, $c$, $1-c$, respectively.

Then, by elementary analysis the tensile plastic resistance $Y$ of the composite assembly is obtainable on an appropriate plane strain upper bound model. If in addition the stretching resistance of the interfaces between the two components is included through the interface energy $\chi$, then the final answer is

$$Y = \frac{2}{\sqrt{3}}[cY_c + (1-c)Y_a] + 2\chi/\lambda \qquad \text{(A-1)}$$

where the last term gives the interface tensile stretching resistance.

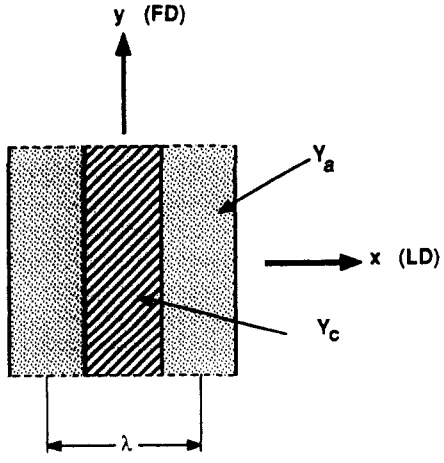


**Figure A1.** Sketch of a stack of crystalline lamellae and associated amorphous region in a state of plastic extensional flow.

When the two contributions to the overall resistance become of comparable magnitude, substantial free energy reduction could be accomplished by the breakup and restructuring of the more sensitive of the two components. This should become possible when

$$\lambda = \frac{\sqrt{3}\chi}{cY_c + (1-c)Y_a} = \frac{\chi}{c\tau_c + (1-c)\tau_a} \qquad \text{(A-2)}$$

where $\tau_c$ and $\tau_a$ are the plastic shear resistances of the crystalline and amorphous components, respectively, and where we have related the shear resistance to the tensile resistance by a Mises yield criterion.

**Acknowledgment.** This research has been supported in parts by a DARPA U.R.I. program under ONR Contract No. N00014-86-K-0768 through MIT and by the Polish Academy of Sciences.

## References and Notes

(1) Oda, T.; Kawai, H. *J. Polym. Sci.* **1965**, *A3*, 1943. O'Leary, K. J.; Geil, P. H. *J. Macromol. Sci., Phys.* **1962**, *B2*, 261.
(2) Bowden, P. B.; Young, R. J. *J. Mater. Sci.* **1974**, *9*, 2034.
(3) Haudin, J. M. In *Plastic Deformation of Amorphous and Semi-Crystalline Materials*; Escaig, B., G'Sell, C., Eds.; Les Editions de Physique: Les Ulis, 1982; p 291.
(4) Lin, L.; Argon, A. S. *J. Mater. Sci.*, submitted for publication.
(5) Peterson, J. M. *J. Appl. Phys.* **1968**, *39*, 4920.
(6) Bartczak, Z.; Argon, A. S.; Cohen, R. E. *Macromolecules*, submitted for publication.
(7) Young, R. J.; Bowden, P. B. *Philos. Mag.* **1974**, *29*, 1061.
(8) Pope, D. H.; Keller, A. *J. Polym. Sci., Polym. Phys. Ed.* **1975**, *13*, 533.
(9) Burnay, G. S.; Groves, G. W. *J. Mater. Sci.* **1978**, *13*, 639.
(10) Argon, A. S. *Philos. Mag.* **1973**, *28*, 39.
(11) Boyce, M. C.; Parks, D. M.; Argon, A. S. *Mech. Mater.* **1988**, *7*, 15.
(12) Hay, I. R.; Keller, A. *Kolloid Z. Z. Polym.* **1965**, *204*, 43.
(13) Peterlin, A. *Colloid Polym. Sci.* **1975**, *253*, 809.
(14) Peterlin, A. In *Polymeric Materials*; Baer, E., Ed.; American Society for Metals: Metals Park, OH; 1975; p 175.
(15) Lee, B.-J.; Argon, A. S.; Parks, D. M.; Ahzi, S.; Bartczak, Z. *Macromolecules*, submitted for publication.
(16) Lin, L.; Argon, A. S. *Macromolecules* **1992**, *25*, 4011.
(17) Song, H. H.; Argon, A. S.; Cohen, R. E. *Macromolecules* **1990**, *23*, 870.
(18) Galeski, A.; Argon, A. S.; Cohen, R. E. *Macromolecules* **1991**, *24*, 3953.
(19) Gray, R. W.; Young, R. J. *J. Mater. Sci.* **1974**, *9*, 521.
(20) Galeski, A.; Argon, A. S.; Cohen, R. E. *Macromolecules* **1991**, *24*, 3945.
(21) Kanig, G. *Kolloid Z. Z. Polym.* **1973**, *251*, 782.
(22) Bartczak, Z.; Argon, A. S.; Cohen, R. E. *Macromolecules*, in press.
(23) Young, R. J.; Bowden, P. B.; Ritchie, J. M.; Rider, J. G. *J. Mater. Sci.* **1973**, *8*, 23.
(24) Hoffman, J. D.; Davis, G. T.; Lauritzen, J. I., Jr. In *Treatise on Solid State Chemistry*; Hannay, N. B., Ed.; Plenum Press: New York, 1976; Vol. 3, Chapter 7.

**Registry No.** Petrothene LS (homopolymer), 9002-88-4.